Proceedings of The 7th International Symposium on Cavitation
CAV 2009
August 17-22, 2009, Ann Arbor, Michigan, USA

CAV2009-0062

NUMERICAL INVESTIGATION OF CLOUD CAVITATION AND CAVITATION NOISE ON A HYDROFOIL SECTION

Jung Hee Seo
Post Doctoral Fellow
Department of Aeronautics and Astronautics
Stanford University
Stanford, California 94305
Email: jhseo@stanford.edu

Sanjiva K. Lele
Professor
Department of Aeronautics and Astronautics
Stanford University
Stanford, California 94305
Email: lele@stanford.edu

ABSTRACT

Partial cavitating flow and cloud cavitation on a hydrofoil section are numerically investigated. A fully compressible, density based homogeneous equilibrium model is employed along with a RANS turbulence model and high-order numerical methods based on a sixth-order central compact scheme and localized artificial diffusivity scheme are used to resolve the cavitating flow and pressure waves generated by cloud cavitation. Predicted results compare well with the experimental measurments for steady/unsteady partial cavitating flows on a NACA66 hydrofoil at cavitation number, σ=1.0-1.4 and angle of attack 6 and 8 degree. Detailed experimental data from the work of Leroux et al. were provided by Prof. J.-A. Astolfi at Institut de Recherche de l'Ecole Navale, France. Numerical visualizations of cloud cavity evolution and surface pressure signals show relatively good agreement with the experimental data. The re-entrant jet flow and pressure wave generated by collapse of cloud cavity are closely investigated. The mechanism associated with two different unsteady dynamics of cloud cavitation observed in previous numerical/experimental study for angle of attack 6 and 8 degree are further explored using the present computational results. The pressure pulse generated by the collapse of bubble cloud and the flow-blockage effect caused by a large cavity cloud are found to be responsible for the shifting of cloud cavitation dynamics.

INTRODUCTION

Severe cavitation noise and erosion damage are caused by cloud cavitation. Formation and collapse of such clouds of cavitation bubbles generate strong pressure waves which are responsible for the noise and erosion. There are several experimental studies for cloud cavitation especially on hydrofoil sections [1–7]. In these experiments, it is observed that the partial sheet cavity is periodically broken-up and rolls up into bubble clouds. The re-entrant jet that flows under the cavity has been believed to be the origin of such cavity destabilization. Pressure wave phenomena is another important feature of cloud cavitation. Reisman et al. [4] investigated the collapse of well-defined and separate cavity clouds for a pitching hydrofoil. Several types of propagating structures (shock waves) which formed in a collapsing cloud were observed by correlating surface pressure measurement with high-speed motion images. Leroux et al. [5, 6] studied partial sheet /cloud cavitation on a stationary hydrofoil. Based on the analysis of surface pressure measurements, they indicated that the pressure wave generated by shedding of cloud cavitation effects the dynamics of cloud cavitation itself. Additionally, the shifting of cloud cavitation dynamics reported in several experiments [3, 6] is also very interesting. However, it is very difficult to measure the re-entrant jet flow inside the cavity and pressure wave phenomena in detail. In this respect, numerical simulation is considered an important tool for close investigation of the flow physics.

The objective of present study is the numerical investigation of cloud cavitation and cavitation noise (pressure wave gener-

ated by cloud cavitation) on a hydrofoil section. In particular, we want to evaluate the ability of simple Reynolds-averaged turbulence model based calculation methods in their unsteady mode in predicting macroscale cavitation phenomena. The density based homogeneous equilibrium model [8] and high-order numerical methods based on a central compact scheme are employed to resolve the cloud cavitation phenomena and the pressure waves generated by cloud cavitation. The governing equations are the compressible Navier-Stokes equations for the gas/vapor-liquid mixture. The two-phase flow physics is treated by a linearly-combined equation of state allowing the compressibility effects in liquid and gas phases. Since the governing equations are hyperbolic, the generation and propagation of the waves can be resolved. The high-order central compact scheme [9] which is widely used in computational aero-acoustics is very efficient and accurate for representing broadband flow variations. However, it cannot capture flow discontinuities because the scheme has no built-in numerical dissipation. In the present study, therefore, we used the localized artifical viscosity/diffusivity proposed by Cook & Cabot [10] and Fiorina & Lele [11], and recently revised and adopted to curvilinear coordinates by Kawai & Lele [12]. This approach limits artificial diffusion to only the unresolved scales and the resolved scales are not affected. For turbulence modeling, the one-equation, Spalart-Allmaras model [13] is applied and the eddy viscosity correction method for two-phase region proposed by Coutier-Delgosha et al. [14, 15] is used.

In the present study, we focused on the partial sheet/cloud cavitation on a NACA66 series hydrofoil (NACA66(mod.)-312 a=0.8) which has been extensively studied experimentally by Leroux et al. [5, 6] and Leroux [7].This geometry has also been numerically studied by Leroux et al. [6] with a barotropic two-phase modeling and Zhou & Wang [16] with the full cavitation model. Zhou & Wang studied the foil at AOA(angle of attack)=6 deg. for stable/unstable partial-sheet cavitation. They focused on the effect of turbulence modeling and their numerical results were in good agreement with experimental measurment. Leroux et al. investigated the two different cloud cavitation dynamics modes exhibited at AOA = 6 and 8 degree numerically and experimentally [6]. Their numerical results also show two different types of dynamics and generally agree with the experiments. The present study covers all the cases studied by Leroux et al. and Zhou & Wang. It includes stable/unstable partial sheet/cloud cavitation and shifting of cloud cavitation dynamics. The scope of present study is, therefore, appropriate to show the feasibility of numerical simulation for its accuracy in predicting various cavitating fow dynamics. The numerical results are compared with experimental data of Leroux et al.(experimental data were provided by Prof. J.-A. Astolfi at Institut de Recherche de l'Ecole Navale, France.). The re-entrant jet flow and pressure wave generated by cloud cavity are investigated more closely than previous studies. Especially, the propagation of pressure wave and their effects on cloud cavitation dynamics are studied in detail in this paper.

FORMULATION AND MODELING

Governing Equations

In this study, we applied a density based homogeneous equilibrium model of Shin et al. [8]. Similar model is used in previous numerical studies [17–19]. In the homogenous medium, the mixture density ρ can be expressed as a linear combination of densities in liquid-phase ρ_l and gas-phase ρ_g:

$$\rho = (1-\alpha)\rho_l + \alpha\rho_g, \tag{1}$$

where α is the void fraction (gas volume fraction). The relation between the local void fraction α and quality (gas mass fraction) Y is given by

$$\rho(1-Y) = (1-\alpha)\rho_l \quad \text{and} \quad \rho Y = \alpha\rho_g. \tag{2}$$

The gas mass fraction Y is the sum of the mass fraction of non-condensable gas Y_{ng} and vapor mass fraction Y_v. Y_{ng} is the air contamination of liquid water and assumed as a constant. The equations of state for a pure liquid [20] and an ideal gas are written as follows:

$$p + p_c = \rho K(T + T_c) \quad \text{for } Y = 0 \text{ (pure liquid)} \tag{3}$$

$$p = \rho RT \qquad \text{for } Y = 1 \text{ (pure gas)} \tag{4}$$

where p and T are the static pressure and temperature, p_c, T_c, K are the pressure, temperature and liquid constant for the liquid state, and R is the gas constant. Using these two equations and the local equilibrium assumption, the equation of state, Eq. (1) for a locally homogenous gas-liquid two-phase medium can be written as

$$\rho = \frac{p(p+p_c)}{K(1-Y)p(T+T_c) + \bar{R}Y(p+p_c)T} \tag{5}$$

where $\bar{R} = (Y_{ng}R_{ng} + Y_vR_v)/Y$ is the averaged gas constant and R_{ng}=287.058 J/(kg K) and R_v=461.5 J/(kg K) are gas constants for air and vapor respectively. The speed of sound for the isothermal condition, a is derived as

$$a^2 = \frac{Y\{\bar{R}(p+p_c) - Kp\} + Kp}{Y\{\bar{R}(p+p_c)^2 - Kp^2\} - \rho K\bar{R}Y(1-Y)p_cT_c + Kp^2} \times \frac{p(p+p_c)}{\rho} \tag{6}$$

The constants p_c, K and T_c for water in Eq. (5) were estimated as 1944.61 MPa, 472.27 J/(kg K) and 3837 K, respectively. The speed of sound estimated by Eq. (6) agrees well with Karplus' [8, 21] experimental data at atmospheric pressure.

Based on the above model, under the isothermal condition, the governing equations for the mixture mass, momentum, and gas-phase mass conservation can be written as

$$\begin{aligned}
&\frac{\partial \rho}{\partial t} + \nabla \cdot (\rho \vec{u}) - \nabla \cdot \vec{J}_\rho = 0 \\
&\frac{\partial \rho \vec{u}}{\partial t} + \nabla \cdot (\rho \vec{u}\vec{u} + p) - \nabla \cdot \tau = 0 \\
&\frac{\partial \rho Y}{\partial t} + \nabla \cdot (\rho \vec{u} Y) - \nabla \cdot \vec{J}_Y = S_e - S_c
\end{aligned} \tag{7}$$

The source terms S_e and S_c in mass fraction equation are the inter-phase mass transfer rates accounting for the local evaporation and condensation. We used the model of Saito et al. [18], which is based on the theory of evaporation/condensation on a plane surface [22].

$$\begin{aligned}
S_e &= C\alpha^2(1-\alpha)(1-Y)\frac{\rho}{\rho_g}\frac{\max(p_v - p, 0)}{\sqrt{2\pi R_v T}} \\
S_c &= C\alpha(1-\alpha)^2\frac{\rho}{\rho_g}\max(Y_v, 0)\frac{\max(p - p_v, 0)}{\sqrt{2\pi R_v T}}
\end{aligned} \tag{8}$$

where p_v is a vapor pressure and C is an empirical model constant and has the dimension of $[m^{-1}]$. Saito et al. [18] suggested the value of $C = 0.1$ based on the test of cavitating flow over a hemispherical/cylindrical object. It has been also shown that the cavitating flow result is not very sensitive to the value of this constant. In this study, therefore $C = 0.1$ is used for all computations. The viscous stress tensor τ and the diffusive fluxes $\vec{J}_\rho$ and $\vec{J}_Y$ are expressed by

$$\begin{aligned}
\tau &= (\mu + \mu_t)(2\mathbb{S}) + (\beta^* - \frac{2}{3}(\mu + \mu_t))(\nabla \cdot \vec{u})\mathbb{\delta} \\
\vec{J}_\rho &= D_\rho^* \nabla \rho, \quad \vec{J}_Y = \rho(D_Y + D_Y^*)\nabla Y
\end{aligned} \tag{9}$$

where $\mathbb{S}$ is a strain rate tensor, μ, μ_t, and D_Y are physical viscosity, eddy viscosity, and mass diffusivity respectively. Variables with asterisk(*) are artificial viscosity and diffusivities that ensure numerical stability for under resolved flows. They act locally and dynamically. Artificial fluid properties take on significant values only in the region where the steep gradient of flow variables exists. For two phase flow, the physical viscosity μ is estimated [23] by

$$\mu = (1-\alpha)(1+2.5\alpha)\mu_l + \alpha\mu_g \tag{10}$$

where μ_l and μ_g are viscosities for liquid and gas phase respectively.

Turbulence Model

Computational modeling of cavitating turbulent flows still remains as an open issue. The detailed mechanisms of the interaction between turbulent flows and cavitation have not yet been clearly revealed especially for the phenomena occuring at small scales. In this study, therefore, we employed simple Reynolds-averaged turbulence model to resolve only the macro-scale unsteady cavitation phenomena. The Spalart-Allmaras model (one-equation, eddy viscosity transport model) is applied as a baseline turbulence model. Neglecting transition terms, the eddy viscosity transport equation is written as

$$\begin{aligned}
&\frac{\partial}{\partial t}(\rho\tilde{\nu}) + \nabla \cdot (\rho\vec{u}\tilde{\nu}) = \rho C_{b1}\tilde{S}\tilde{\nu} \\
&+ \frac{1}{\sigma_\nu}\left\{\nabla \cdot [(\mu + \rho\tilde{\nu})\nabla\tilde{\nu}] + \rho C_{b2}|\nabla\tilde{\nu}|^2\right\} - \rho C_{w1} f_w \left(\frac{\tilde{\nu}}{d}\right)^2
\end{aligned} \tag{11}$$

and $\nu_t = \tilde{\nu} f_{v1}$. Coefficients and damping functions are given in Ref. [13]

In previous studies, it has been reported that the unsteady cloud cavitation phenomena were not captured properly with the standard turbulence models based on incompressible flow analysis. Coutier-Delgosha et al. [15] and Zhou & Wang [16] observed that an excessive generation of eddy viscosity inside the cavity prevented the development of re-entrant jet flow which plays the major role on the instability of partial sheet cavity. The standard Spalart-Allmaras model used in the present study also showed this problem. As a remedy to such a problem, Coutier-Delgosha et al. [14] proposed an eddy viscosity correction for high void fraction region:

$$\mu_t = [\rho_g + (\rho_l - \rho_g)(1-\alpha)^n]\nu_t \tag{12}$$

where $n >> 1$ is the modeling constant. This correction significantly decreases the eddy viscosity value inside the cavity(high void fraction region). They applied this correction method to the computation with RNG k-ε model and obtained good agreement with the experiment for cloud cavitation shedding in a venturi-type duct. Coutier-Delgosha et al. argued that this simple eddy viscosity correction is virtually equivalent to the compressibility correction for turbulence models and showed that the compressibility correction also results the decrease of eddy viscosity value for high void fraction region [15]. Leroux et al. [6] and Zhou & Wang [16] used the same correction method and RNG k-ε turbulence model for the computation of cloud cavitation on a NACA66 hydrofoil section, and also obtained satisfactory results. In this study, we applied this correction method

with the Spalart-Allmaras model, and $n = 3$ suggested by Zhou & Wang [16] for the same geometry(NACA66).

Numerical Method

All the governing equations are transformed into a generalized curvilinear coordinates and spatially discretized in computational domain with a sixth-order central compact scheme [9]. Time integration is performed with a four-stage Runge-Kutta method and the eighth-order spatial filtering proposed by Gaitonde et al. [24] is applied after each final Runge-Kutta step. For out-going acoustic waves, Freund's buffer-zone type absorbing boundary condition [25] is applied at open boundaries.

The artificial viscosity and diffusivity in Eq. (9) are written for the curvilinear coordinates according to Kawai and Lele [12].

$$\beta^* = C_\beta \rho \overline{\left[\Delta_\xi^6(\xi_x^2+\xi_y^2)^3\frac{\partial^4 S}{\partial\xi^4} + \Delta_\eta^6(\eta_x^2+\eta_y^2)^3\frac{\partial^4 S}{\partial\eta^4}\right]} \tag{13}$$

$$D_\rho^* = C_\rho \frac{a_0}{\rho}\overline{\left[\Delta_\xi^5(\xi_x^2+\xi_y^2)^3\frac{\partial^4 \rho}{\partial\xi^4} + \Delta_\eta^5(\eta_x^2+\eta_y^2)^3\frac{\partial^4 \rho}{\partial\eta^4}\right]} \tag{14}$$

$$D_Y^* = C_{Y1}\frac{a_0}{Y_0}\overline{\left[\Delta_\xi^5(\xi_x^2+\xi_y^2)^3\frac{\partial^4 Y}{\partial\xi^4} + \Delta_\eta^5(\eta_x^2+\eta_y^2)^3\frac{\partial^4 Y}{\partial\eta^4}\right]} + C_{Y2}\frac{a_0}{Y_0}\overline{Y_v[1-H(Y_v)]\Delta_Y} \tag{15}$$

where S is the magnitude of strain rate tensor S, a_0 is ambient speed of sound, and H is the Heaviside function. The fourth derivatives in above equations are evaluated with the fourth-order central compact scheme [9]. The overbar denotes Gaussian filtering and the approximate truncated-Gaussian filter of Cook and Cabot [10] is applied. Δ_ξ and Δ_η are the grid spacing in the physical space along the grid line, and Δ_Y is defined by

$$\Delta_Y = \frac{\left|\frac{\partial^4 Y}{\partial\xi^4}\right|\Delta_\xi + \left|\frac{\partial^4 Y}{\partial\eta^4}\right|\Delta_\eta}{\sqrt{\left(\frac{\partial^4 Y}{\partial\xi^4}\right)^2 + \left(\frac{\partial^4 Y}{\partial\eta^4}\right)^2 + \varepsilon}} \tag{16}$$

where ε is a small number to prevent division by zero. The user-specified constants are set to $C_\beta = 1$, $C_{Y1} = 0.01$, $C_{Y2} = 100$ (values suggested by Kawai and Lele [12]), and $C_\rho = 0.1$.

Geometry

The geometry of a NACA66 series hydrofoil section (NACA66(mod.)-312 a=0.8, profile given in Ref [5]) is considered. This geometry has been extensively studied experimentally by Leroux et al. for a partial sheet/cloud cavitation. In the present numerical study, we tried to reproduce their water tunnel experiment. In the experiment, the hydrofoil chord length was

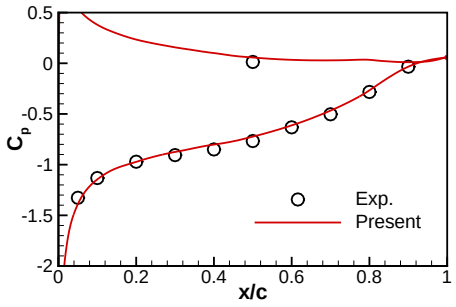

Figure 1. Pressure coefficients for a non-cavitating condition at AOA=6 deg. Experimental data from Ref. [7] provided by Prof. J.-A. Astolfi.

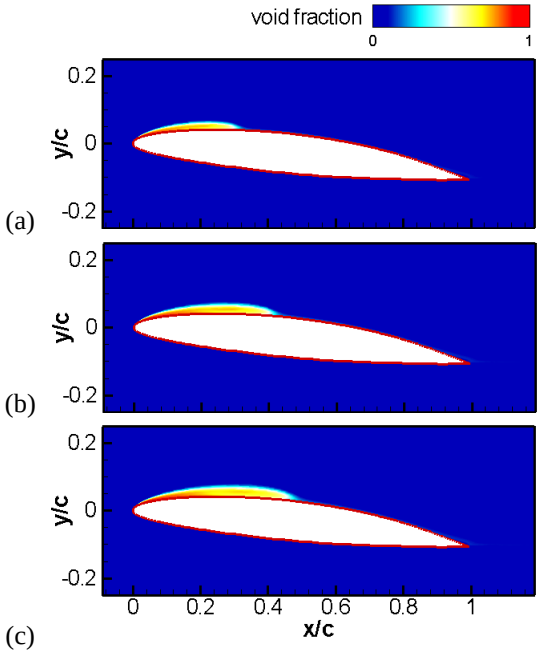

Figure 2. Cavity shapes for (a) σ =1.4, (b) 1.35, and (c) 1.29; void fraction contours.

$c = 0.150$ [m], and the foil was fixed within 1 [m] long and 0.192 [m] wide square cross test section. The flow Reynolds number based on a chord length was about $Re_c = \rho_0 u_0 c/\mu = 8\times10^5$. The angle of attack $6-8$ degree was tested. The computational domain respects the experimental test section, but it is simplified to a two-dimensional problem. A C-type 801×81 grid points are used and the suction surface of hydrofoil is covered with 250 grid points. The y^+ values of wall adjacent cell's centroid are within 1-2. The present grid resolution is determined based on grid-convergence studies for a non-cavitating flow. A slip-wall boundary condition is used for upper and lower walls. Pressure and velocity are fixed at the inlet and absorbing boundary condi-

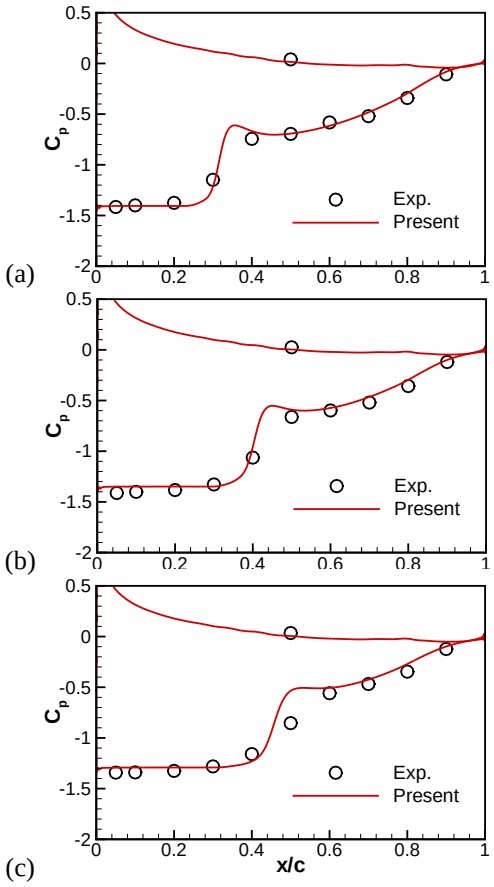

Figure 3. Comparisons of pressure coefficients for a) σ =1.4, (b) 1.35, and (c) 1.29. Experimental data from Ref. [5] provided by Prof. J.-A. Astolfi.

tion is applied at the inlet and outlet.

RESULTS AND DISCUSSION

At first, the simulation for a non-cavitating condition is performed to verify the turbulent flow model and geometry modelings (hydrofoil and test section). The pressure coefficient ($C_p = (p - p_0)/\frac{1}{2}\rho_0 u_0^2$) distributions for AOA(angle of attack)=6 deg. are shown in Fig. 1 with the experimental measurement (all the experimental data presented in this paper are from Leroux et al. [5, 6] and Leroux [7]). The present result agrees nicely with the experimental data. The flow on the pressure surface is expected to be non-cavitating and most of unsteady, cavtating flow phenomena occur on the suction surface. This is why the pressure data was measured at only one point on the pressure surface.

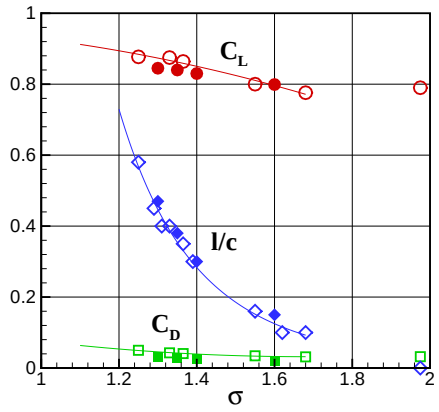

Figure 4. Comparison of drag, lift coefficients(C_D,C_L), cavity length (l/c); hollowed symbols: measurement, filled symbols:present computation. Experimental data from Refs. [5, 7] provided by Prof. J.-A. Astolfi.

Stable Partial Sheet Cavitations

In the experiment of Leroux et al., stable development of partial sheet cavity is observed for cavitation number $\sigma = (p_0 - p_v)/\frac{1}{2}\rho_0 u_0^2 > 1.25$ (or developed cavity length $l/c < 0.5$) at AOA=6 deg. and $Re_c = 8 \times 10^5$. Computations of these cases are carried out by varying $\sigma = 1.25 - 1.4$. Computed cavity shapes are shown in Fig. 2. For these conditions, quasi-steady state, stable cavitation is obtained from numerical simulations. Fig.3 shows calculated pressure coefficient distributions and good agreement with the measurments can be noted. Although the main cavity remains stable, small vapor shedding at the cavity closure region was observed in the experiment. Such small scale structures are, however, not expected to be resolved with the present RANS-based turbulent flow model. The predicted lift and drag coefficients and cavity length (measured from the cavity shape outline defined by contour at $\alpha = 0.1$) are shown in Fig.4 for stable cavity cases. These values compare well with the measured data.

Unstable Cavity and Cloud Cavitation

For $\sigma < 1.25$ (or $l/c > 0.5$) the partial sheet cavity is found to be unstable. The sheet cavity brakes and rolls up, and is then shed off and finally collapses. This process is quasi-periodic and its frequency is determined as about 3.5 [Hz] in the experiment. This type of cloud cavitation is also exhibited in the numerical simulation at $\sigma = 1.2$. Figure 5 shows the time evolution of cloud cavitation computed with the present model: The sheet cavity is developed up to x/c=0.7 (a-c). During this stage, the re-entrant flow developes, and it breaks the sheet cavity (d). This re-entrant flow is clearly visible in the numerical simulation (it will be discussed further in a later section). The rear part of cavity then rolls up into a large cloud while the front part disappears (e).

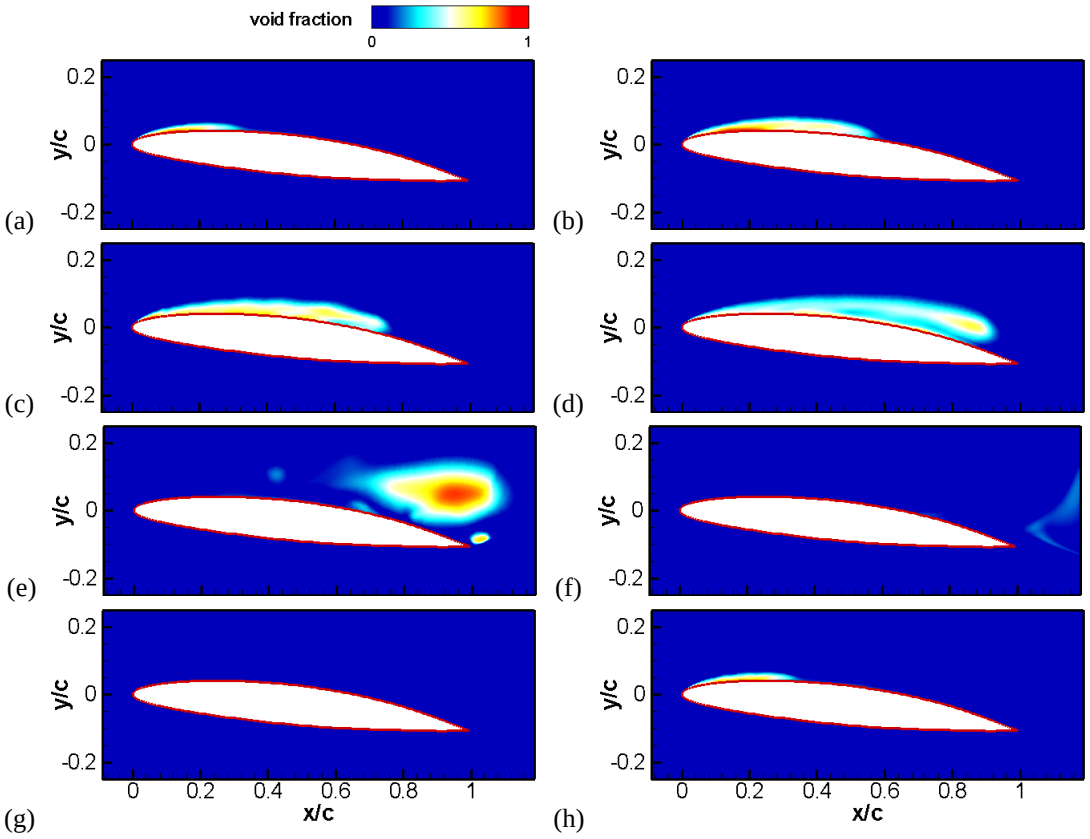

Figure 5. Time evolution of void fraction for $\sigma = 1.2$ and AOA=6 deg. (Time interval between images is about 1/25 [sec]).

This cloud is shed off and finally collapses. The entire foil is cavitation-free for a while (f-g), and new sheet cavity starts to develop again (h). The predicted frequency of cavity fluctuation, 3.7 [Hz] is in acceptable agreement with the measured value. The numerical visualization looks quite similar to photographs from the experiment [5]. Surface pressure signals at x/c= 0.3,0.5, and 0.7 on the suction surface are plotted in Fig. 6 along with the measurements. Pressure fluctuation on the suction surface is dominated by the growth and destabilization of the cavity. Overall, the pressure signal follows the measurment well, but some differences are noticeable. In the present simulation, the disappearance of the front-part of broken sheet cavity occurs a little bit early than the experiment, and the cavitation-free duration is also a bit longer. Due to this, the predicted pressure signal at x/c=0.3 is quite different from the experiment. One possible reason of this disagreement is that cavitation inception near the foil leading edge is initiated by stream-wise vortex cores which is not resolved in present 2D simulation. Finger-like shape of leading edge cavitation caused by stream-wise vortex is clearly visible in experimental photographs [6, 7]. In the numerical simulation, leading edge cavitation disappears more easily due to the absence of such three-dimensional flow features. Also, the small vapor shedding which is observed just before the main cloud shedding in the experiemnt is not captured in the present simulation.

It is also interesting to investigate pressure fluctuation on the pressure side. The pressure fluctation at x/c=0.5 (on the pressure side) is shown in Fig. 7. Comparing to the measurment, however, it is found that the present computation over-predicts the magnitude of fluctuations. This could be due to the over-correlated cloud structure caused by two-dimensional flow assumption. Note that pressure fluctuations are plotted using different scales for a qualitative comparison only. Both traces of pressures decrease just before the cavity destabilization (marked by (3) around 0.42 [sec]). A rarefaction wave generated by the low pressure core of cloud cavity near the trailing edge could be the source of this pressure decrease, as suggested by Song and Qin [26]. They also suspected that it causes the shifting of stagnation point at the nose of a hydrofoil. Leroux et al. [5] argued that the shifting of stagnation point is equivalent to a variation of angle of attack and related the pressure signal on the pressure side to the equivalent change of angle of attack. In order to investigate such a phenomena, overall pressure fields around a hydrfoil are examined in Fig. 8. The low pressure core near the trailing edge corresponds to the cloud cavity. As this low pres-

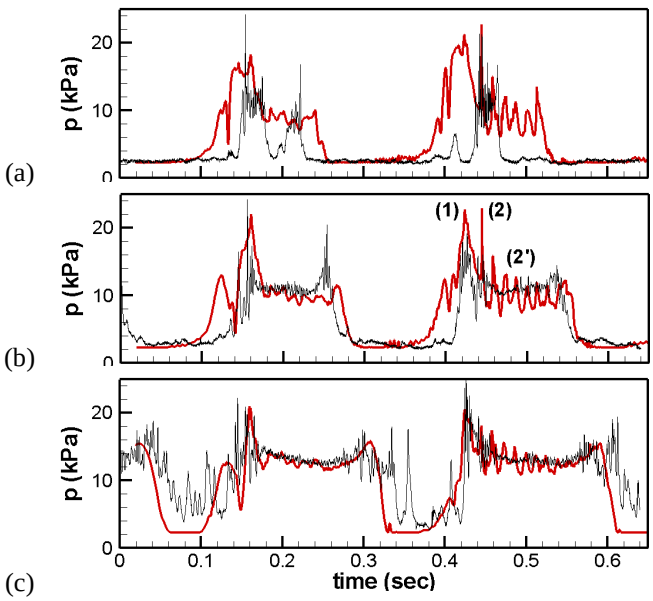

Figure 6. Surface pressure signals at (a) x/c = 0.3, (b) 0.5, and (c) 0.7; red: present computation, black: experimental measurment. Experimental data from Ref. [5] provided by Prof. J.-A. Astolfi.

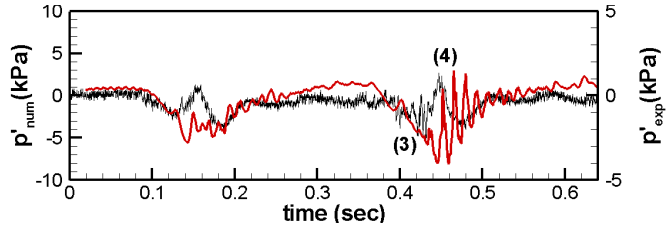

Figure 7. Pressure fluctuation at x/c = 0.5 on the pressure surface; red: present computation, black: experimental measurment. Experimental data from Ref. [5] provided by Prof. J.-A. Astolfi.

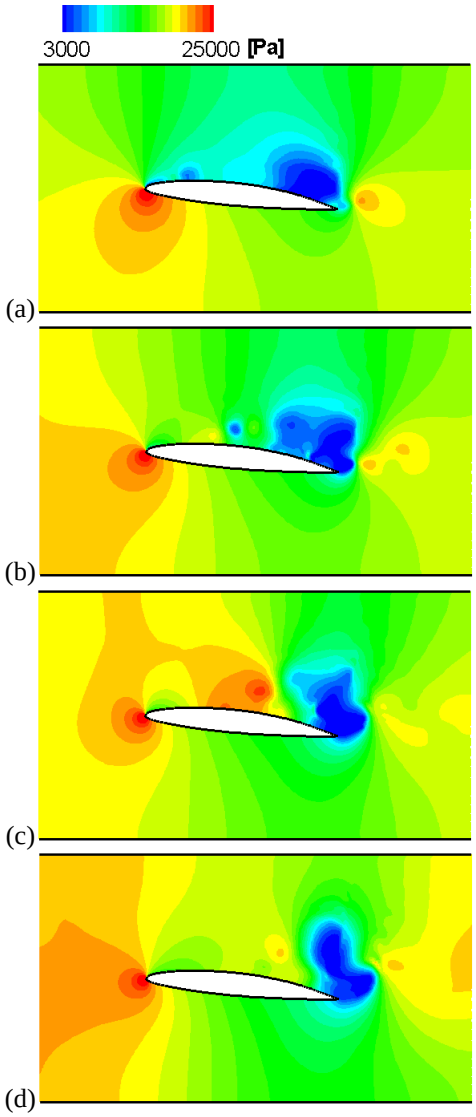

Figure 8. Pressure field around a hydrofoil; (a) time = 0.39 [sec], (b) 0.41 [sec] (frame (e) of Fig.5), (c) 0.42 [sec], and (d) 0.43 [sec]. 20 Contour levels between 3-25 [kPa].

sure core passes over the trailing edge, the pressure under the foil decreases while the upper surface pressure increases. As a result, the stagnation point moves in the direction of decreasing equivalent angle of attack. This is consistent with the analysis of Leroux et al. As discussed by them, a decrease in the equivalent angle of attack is responsible for the destabilization of cavity and also the collapse of the residual cavity (front part of broken sheet cavity). In Fig.8 (c), one can see a sudden strong pressure increase on the suction surface caused by the destabilization and collapse of the residual cavity. This corresponds to the pressure peak in time signal shown in Fig.6 (marked by (1)) that appears both in numerical and experimental pressure traces. This is a large-scale pressure fluctuation and it propagates both up- and downstream in the tunnel. The decrease of equivalent angle of attack prevents the development of new sheet cavity and makes the entire foil cavitation free for a while. After the shedding of cloud cavity is completed, the stagnation point returns to its orginal position and new sheet cavity starts to develop.

Another interesting pressure wave can be found in the signal on the pressure surface and is marked by (4). Instead of this sudden pressure increase observed in experimental signals a train of sharp peaks are observed in the numerical results. By investigating computational result more closely, it is found that a strong pressure wave generated by the partial collapse of shed cloud cavity is responsible for these peaks. In the numerical re-

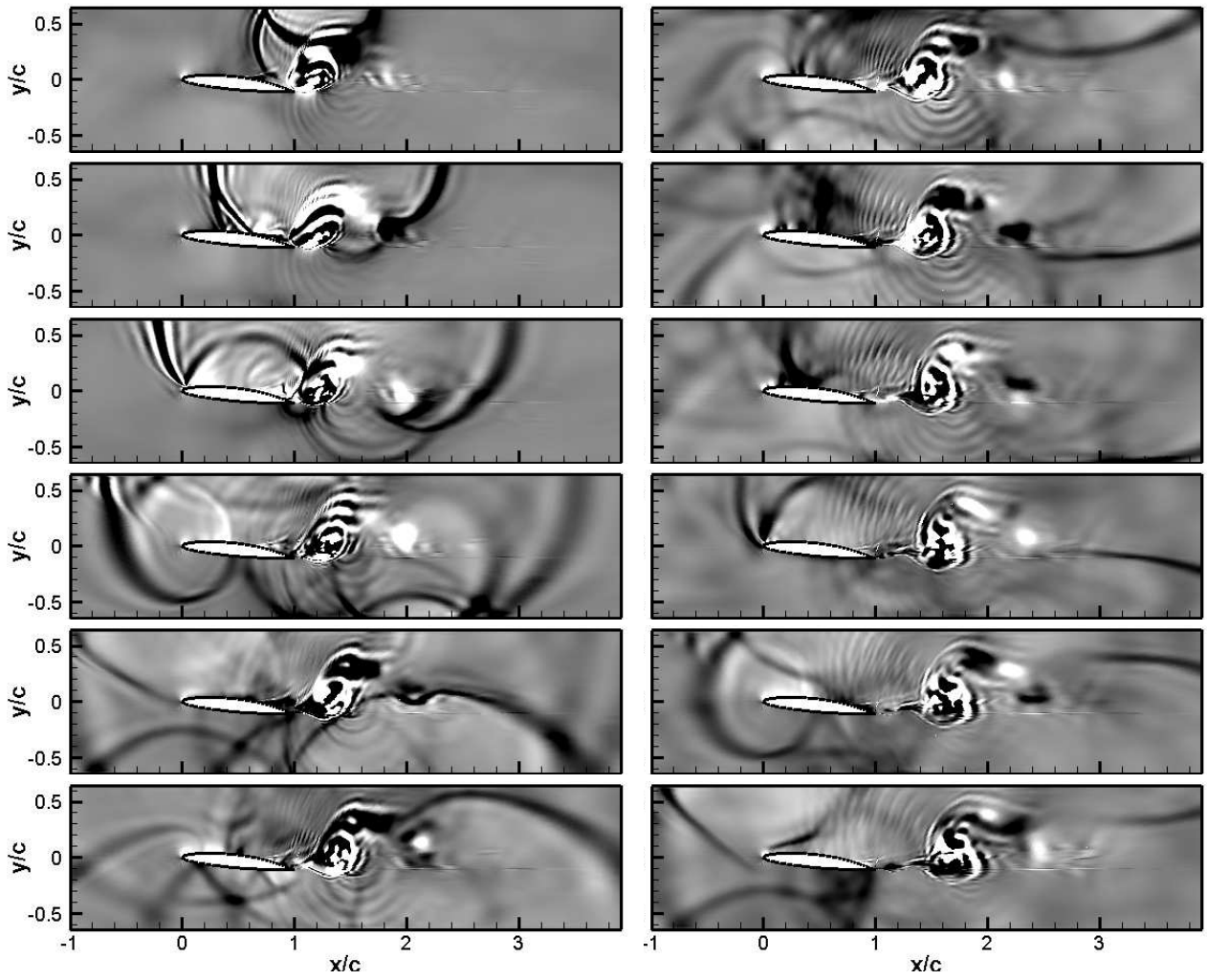

Figure 9. Pressure wave generated by partial collapse of cloud, non-dimensionalized dilatation rate, $(\nabla \cdot \vec{u})c/u_0$ (between -0.1 and 0.1) contours for time = 0.442 - 0.464 [sec], interval: 0.002 [sec] (from upper to bottom and left to right).

sults, the cloud cavity is shed from the foil and partially collapses in the near wake just after the shedding and generates a strong pressure wave. After the partial collapse, cloud forms a well-correlated circular shape and is convected further downstream. The strong pressure wave generated by the partial collapsing is visualized in Fig.9. The collapse occurs at the position a bit upper the foil suction surface. As one can see in the first frame of Fig. 9, the pressure wave hits the upper wall and is reflected. The wave is reflected again by the foil (it generates peaks on the suction surface pressure signal; marked by (2)) and also deflected at the leading and trailing edge. The wave is successively reflected by upper and lower walls and also foil surface. These reflected waves are responsible for the train of peaks observed in both suction(2') and pressure surface(4) pressure signal. The present two-dimensional wave and geometry may cause these coherent wave reflections, which are not observed in the measurment. Nevertheless, the pressure wave generated by the collapse of cloud can explain the pressure wave phenomena observed in surface pressure signals. Note also many secondary waves apparent in Fig.9. Some of these may be artifacts of insufficient grid resolution.

Transition of Cloud Cavitation Dynamics

Leroux et al. observed two distinct types of cavity self-oscillation dynamics at the angle of incidence, AOA=6 and 8 deg in the experiment [6, 7]. For AOA=6 deg, the frequency of cavity oscillation is almost constant of about 3.5 [Hz]. They called this low-frequency cavity oscillation 'dynamics 1'. The frequency increases suddenly at a transition angle of about 7.5 deg. At AOA=8 deg and σ=1.27, a much larger oscillation fre-

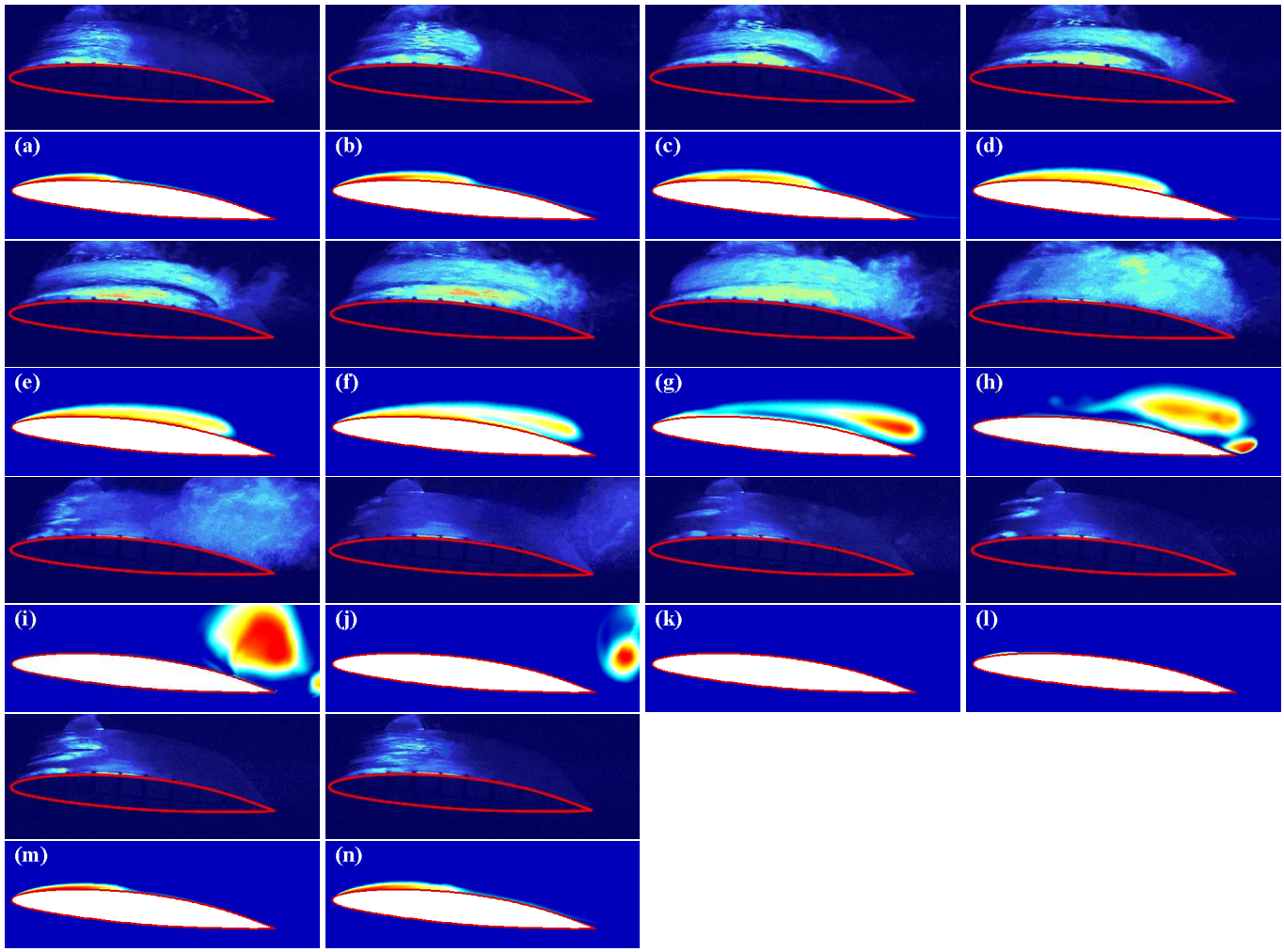

Figure 10. Visualization of cloud cavitation for dynamics 1. Time interval between images: 1/50 [sec]. Experiment (upper images), AOA=6 deg, $\sigma = 1.00$. Computations (lower images), instantaneous void fraction, AOA=6 deg, $\sigma = 1.05$. Experimental data from Ref. [6] provided by Prof. J.-A. Astolfi.

quency of 18 [Hz] is observed for which Strouhal number based on a cavity length is about St_l=0.3. This high-frequency behavior was called 'dynamics 2'. They related this frequency shifting to a parameter $\sigma/2(\alpha-\alpha_0)$($\alpha$ is angle of attack) and obtained results consistent with the analysis of Arndt et al. [3]. In the present numerical simulations, these distinct cavity oscillation frequencies are captured, which allows further exploration of their dynamics.

The numerical simulation at AOA=6 deg and σ=1.05 yields 'dynamics 1'. In the experiment, the cavity oscillation frequency is almost constant (about 3.5 [Hz]) at AOA=6 deg and σ=0.99-1.25. The frequency predicted with numerical simulation increases very slightly, 3.7-3.8 [Hz] for σ=1.05-1.20. For a cavitation number lower than 1.05, however, the frequency increases significantly, i.e. 'dynamics 2' is obtained. The numerical visualization of cloud cavitation is presented in Fig.10 along with the experimental photographs. Overall, the process of sheet cavity destabilization and cloud shedding is not much different from the case discussed earlier for σ=1.2. Visualization with smaller time interval shows the following stages: development of sheet cavity (a-e), cavity destabilization (f-g), formation of cloud and collapse of residual cavity (h), detachment and shedding of main cloud (i-j), cavitation free flow (k), development of new sheet cavity (l-). Some discrepancies between numerical and experimental result are the following. Shedding of secondary cloud (small vapor structure) identified in the experiment during (e-h) is not resolved probably due to turbulence model. The residual cavity disappears bit earlier and slight growth of residual cavity (up to x/c=0.3) after shedding of main cloud (during j-k) is not observed in the present computation. As discussed above for $\sigma = 1.2$ case, the absence of stream-wise vortical structure

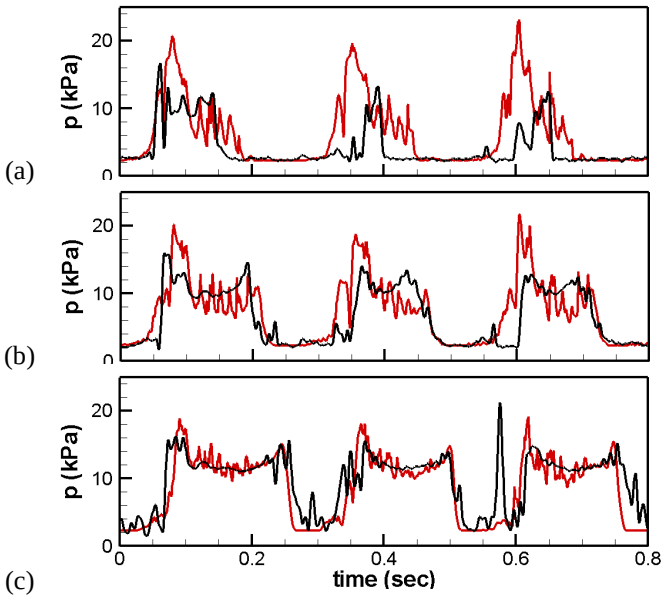

Figure 11. Surface pressure signals for 'dynamics 1' at (a) x/c = 0.3, (b) 0.5, and (c) 0.7; red: present computation, black: experimental measurment. Experimental data from Ref. [6] provided by Prof. J.-A. Astolfi.

near the leading edge due to the two-dimensional flow assumption could be the reason for this. In experimental photographs (j-l), one can see that the residual cavity near the leading edge has finger-like shape rather than sheet (see also top view images in Ref. [6]).

Surface pressure signals at x/c=0.3, 0.5, and 0.7 for suction side are plotted in Fig.11 for both numerical and experimetal results. The numerical result agrees well with the experiment in amplitude and period. The disagreement at x/c=0.3 is mainly due to the aforementioned different behavior of residual cavity near the leading edge. The peak shown in the experimental signal at x/c=0.7 is caused by secondary cloud shedding. Similary to the $\sigma = 1.2$ case, the rarefaction wave by the low pressure core of main cloud and the shifting of stagnation point (decrease of equivalent angle of attack) are still observed at $\sigma = 1.05$. The pressure wave generated by partial collapse of cloud is also exhibited and this generates a train of sharp peaks in the surface pressure signals.

Cloud cavitation in 'dynamics 2' regime is studied for AOA=8 deg and $\sigma = 1.27$, and the results are compared with the experiment. Fig.12 presents visualizations of 'dynamics 2' cloud cavitation. The cycle can be depicted as follows: sheet cavity developes up to the maximum length (about 60% of the chord) (frame (a)); re-entrant jet flows up-stream (b) and cuts the sheet cavity at about 10% of chord (c); the sheet cavity rolls-up into cloud (d-e); the cloud convects and collapses while the residual cavity grows again (f-h). Strong vapor structures (reds) found at the span-ends in experimental pictures are result of side-wall effects. The overall unsteady process is well reproduced by the numerical simulation as shown in Fig.12. The cavity self-oscillation frequency is determined as about 17.3 [Hz], which is in good agreement of measured value 18 [Hz]. Surface pressure signals are shown in Fig.13 with phase averaged experimental data for this high-frequency phenomena. The numerical results are in acceptable agreement with the experimental ones. In dynamics 2, the shifting of stagnation point is not exhibited, but the pressure wave generated by the collapse of cloud is observed and it sets up small peaks on the surface pressure signal (see Fig.13(b)).

The origin of flow instability for the cavity break down and resulting cloud cavitation is associated with the re-entrant jet that flows under the cavity from its rear part to its upstream end. This is found in the present computation also. The development of re-entrant jet flow for dynamics 2 is examined in Fig.14. One can clearly see the re-entrant flow plotted with blue vectors and vortex sheet beneath cavity interface. The magnitude of developed re-entrant flow increases up to 70% of free-stream velocity at x/c=0.1 just before the sheet cavity break (t=0.0587, see Fig.16(b)). It sets up a strong shear layer exhibited in the figure. Eventually, an instability arises in the shear layer at the upstram position and it breaks the vortex sheet and also the sheet cavity. Avellan et al. [27] and Kjeldsen [28] analyzed Kelvin-Helmoltz instability of the shear layer around the cavity interface. In the up-stream region, the shear layer meets the cavity interface across which the fluid density changes rapidly. The strong enough shear layer formed by counter-flow with different density is subjected to 'absolute' shear layer instability investigated by several researchers [29, 30]. According to Jendoubi & Strykowski [30], the criteria of absolute instability for free shear layer is velocity ratio, $R = (u_1 - u_2)/(u_1 + u_2) > 1.315$ at density ratio, $S = \rho_2/\rho_1$=1 (subscripts 1 and 2 denote values at the upper and lower of the shear layer respectively), and $R >$1.0 at S=0.1. The velocity ratio, R and density ratio, S of the present shear layer formed by re-entrant flow shown in Fig.14 are computed at two different upstream positions, x/c=0.1 & 0.3, and presented in Fig.15. The solid line is the criteria of absolute instability given by Jendoubi & Strykowski. Since the present shear layer is near the viscous no-slip wall, critical values might be slightly different from the result of free shear layer. But most of R, S values are located near the critical line in the sheet cavity developing stage. At t=0.0587, the velocity ratio at x/c=0.1 rapidly increases to R=3 with the development of re-entrant jet flow, and this is strong enough velocity ratio to cause the absolute instability of shear layer. The development of this instability at upstream position breaks the shear layer and thus sheet cavity (Fig.14(e)). More detailed numerical studies for this problem would be much more interesting, since the present numerical simulation is performed in 2D with RANS-based turbulence model. Similar re-entrant jet flow is also observed for dynamics 1 and the cavity destabiliza-

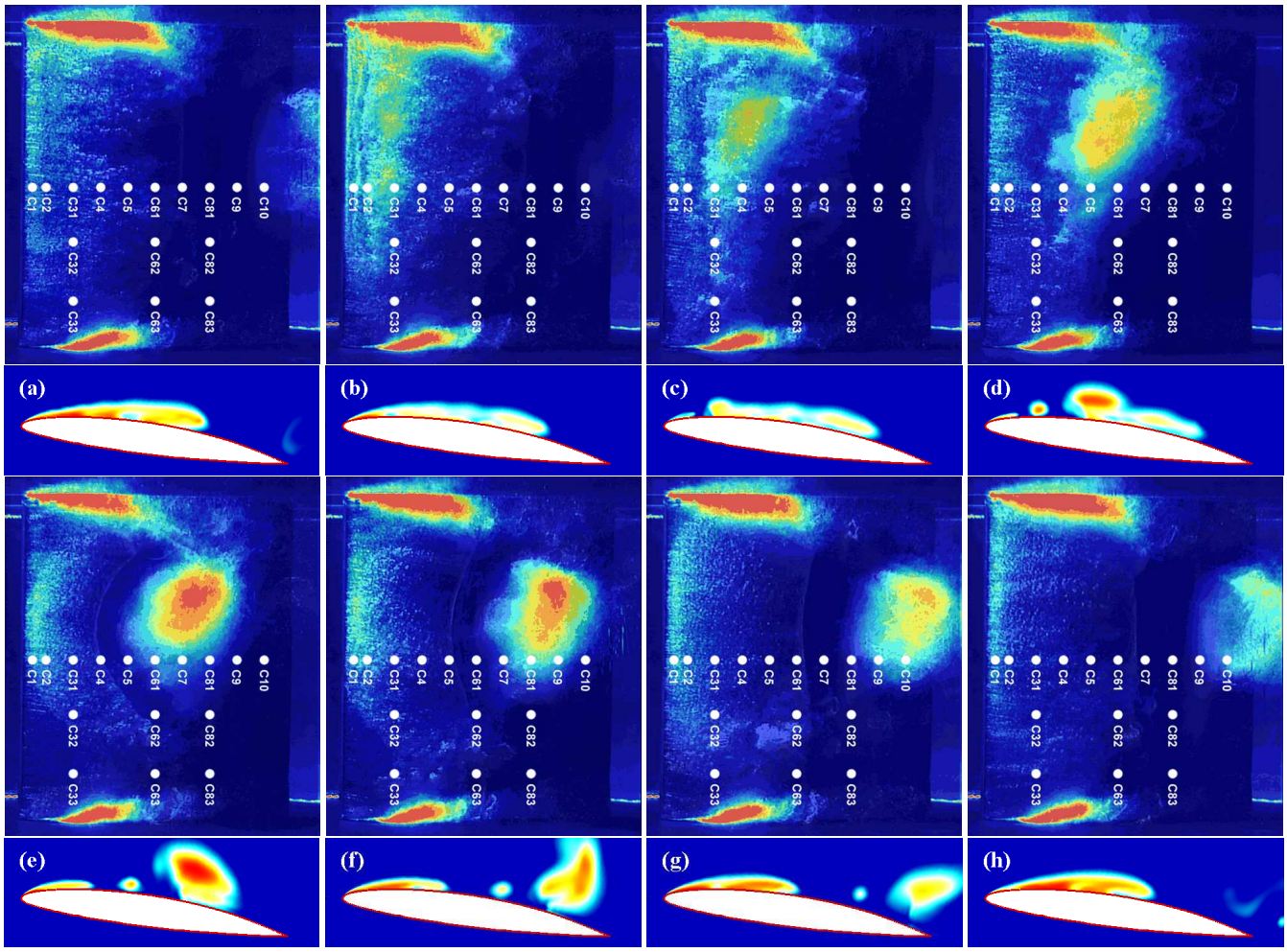

Figure 12. Visualization of cloud cavitation for dynamics 2, AOA=8 deg, $\sigma = 1.27$. Time interval between images: 1/144 [sec]. Top view images (upper) for experiment, side view (lower) for the present simulation, instantaneous void fraction. Experimental data from Ref. [6] provided by Prof. J.-A. Astolfi.

tion of dynamics 1 is triggered by the re-entrant jet flow. The re-entrant jet strength (maximum velocity magnitude of reverse flow under the cavity) is shown in Fig.16 as a function of distance from the leading edge with time increament for both dynamics 1 and 2. It can be seen that the re-entrant jet strength gets stronger as sheet cavity is developing. For a comparison, measured values of Pham et al. [2] (but for a different hydrofoil) are also shown in Fig.16. The present values are consistent with the result of Pham et al. The velocity of the re-entrant jet is of the same order of magnitude as the free stream velocity and increases with the distance from the leading edge [2].

Discussion on the Shifting of Dynamics

The main difference between dynamics 1 and 2 is the frequency of unsteady cloud cavitation. Although the formation of cloud cavity is triggered by the re-entrant jet in both cases, the frequency of dynamics 1 (3.5 [Hz]) is much lower than one of dynamics 2 (18 [Hz]). As one can see in experimental/numerical visualization, for dynamics 2, new sheet cavity starts to develop just after the roll-up of cloud. So one can see both cloud and partial-sheet cavity at the same time on several frames. For dynamics 1, however, the new sheet cavity does not grow well after the roll-up of cloud. The development of new sheet cavity is suppressed until the cloud is compeletly shed off from the foil. This suppression of new sheet cavity development increases the entire unsteady period. Therefore, it is important to investigate the mechanism which causes the suppression of sheet cavity growth for dynamics 1.

Leroux et al. [6] argued, based on the investigation of their numerical results, that the strong pressure wave generated by the collapse of cloud is responsible for such phenomena. They ob-

served very strong pressure wave (its peak value was $C_{p,max}$=28, about 400 [kPa]) caused by the cloud collapse at down stream of the trailing edge (x/c=2.8) for dynamics 1. This pressure wave propagated upstream (its magitude reduced to $C_{p,max}$=3.2 at the trailing-edge) and interacted with the sheet cavity. For dynamics 2, they found that the peak value of similar pressure wave was just $C_{p,max}$=8 (and reduced to 0.8 at the trailing-edge), which was much smaller than dynamics 1. So, they concluded that this different intensity of pressure wave caused the different dynamics.

As shown in above section, the pressure wave caused by the cloud collapse is also observed in the present computation. The pressure wave at the time when it passes the foil is shown in Fig.17 for both dynamics 1 and 2. The pressure wave of dynamics 1 is clearly much stronger than dynamics 2. The strength of pressure wave shown in Fig.17(a) is about 5000 [Pa] and strong enough to suppress cavity development. It is observed that the sheet cavity starts to develop only after this wave propagates out. On the other hand, the pressure wave strength is just about 500-1000 [Pa] for dynamics 2. As one can see in Fig.17(b), the pressure wave is hitting the sheet cavity, but the cavity is not much affected. The different strength of pressure wave might be caused by the size of collapsing cloud. The size of cloud cavity for dynamics 1 is bit larger than dynamics 2 and its collapse generates more strong pressure wave. Consistent with Leroux et al., the stronger pressure wave caused by cloud collpasing for dynamics 1 could be the reason of the suppression of sheet cavity development. However, this pressure wave phenomena has not been confirmed by experiments.

The pressure wave discussed above can be considered as the mechanism that delays the development of new sheet cavity after the shedding of cloud. In Fig.10, however, the sheet cavity disappears and is suppressed just after the forming of cloud. Additional possible reason for the suppression of sheet cavity development might be related to the shifting of stagnation point observed for AOA=6 deg. only. As mentioned in earlier section, when the cloud reaches at the trailing edge, the stagnation point moves in the direction of decreasing equivalent angle of attack, and it returns to its orginal position after the cloud is shed off. The rarefaction wave caused by low pressure core of cloud was considered as the reason of this shifting of stagnation point. The decrease of equivalent angle of attack also means the increase of pressure on the suction side. In fact, it has been observed in the numerical result that the pressure on the suction surface near the leading edge increased up to 13-15 [kPa] after the forming of cloud (but before its shedding and collapse). This pressure increase can explain the shifting of stagnation point and the suppresion of sheet cavity development, but the source of the pressure increase should be addressed. Investigating numerical results closely, we suspect that a blockage effect due to the large cavity cloud and subsequent velocity field change are also responsible for such pressure increase. As mentioned by Song & Qin [26], cloud is a large eddy containing small cavitation bubbles. For

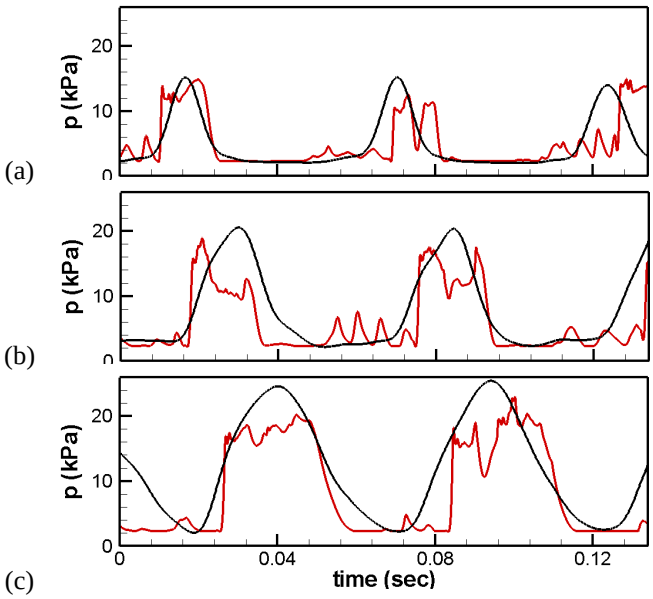

Figure 13. Surface pressure signals for 'dynamics 2' at (a) x/c = 0.3, (b) 0.5, and (c) 0.7; red: presnet computation, black: experimental measurment(phase averaged over 86 synchronized series of three period). Experimental data from Ref. [6] provided by Prof. J.-A. Astolfi.

dynamics 1, the size of cloud is about 0.4c. Considering relatively small tunnel size (h/c=1.28, where h is the tunnel height), this large vortical structure can cause a flow-blockage effect. The instantaneous velocity fields at the time when sheet cavity is developing and it rolled-up into cloud are shown in Fig.18(a) for dynamics 1. One can see clear large vortical structure rotating clock-wise around the cloud. This vortical structure has severe negative velocity near the foil surface. When sheet cavity is developing, the stream wise velocity near the leading edge suction surface is about $1.5u_0$, but it decrease to about $1.1u_0$ due to the vortical structure of cloud. This drop of dynamic pressure increases static pressure significantly, which causes the shifting of stagnation point and suppresses the sheet cavity development. The velocity fields for dynamics 2 are also shown in Fig.18(b). Similar vortical structure around the cloud is observed, but its size and negative velocity region are smaller than dynamics 1. Therefore, it does not make much flow-blockage effect.

CONCLUSIONS

Partial cavitating flow and resulting cloud cavitation on a NACA66 hydrofoil are numerically investigated with a density based homogeneous equilibrium model and high-order numerical methods based on a sixth-order central compact scheme and the localized artificial diffusivity scheme. Applying Spalart-Allmaras turbulence model and eddy viscosity correction method

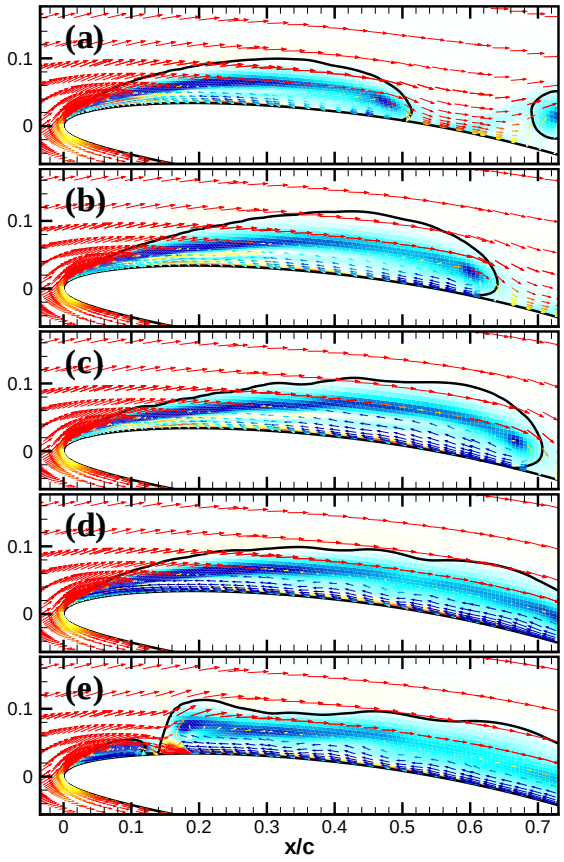

Figure 14. Development of re-entrant jet flow and break of sheet cavity, (a) t=0.0379, (b) 0.0448, (c) 0.0517, (d) 0.0587, and (e) 0.0656. Colors are vorticity contours. Every fourth vectors are plotted. Black line represents cavity shape defined by a contour at α=0.1.

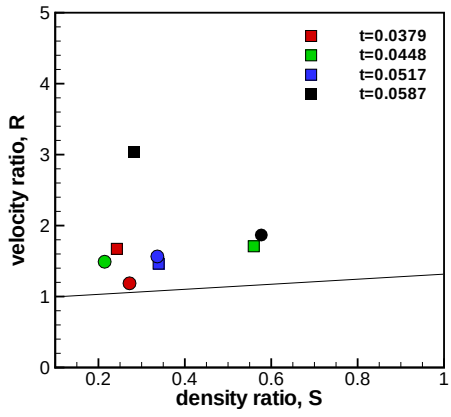

Figure 15. Velocity and density ratio of shear layer formed by re-entrant flow. $R = (u_1 - u_2)/(u_1 + u_2), S = \rho_2/\rho_1$, (subscripts 1 and 2 denote values at the upper and lower of the shear layer respectively). Square symobos: x/c=0.1, circles: x/c=0.3. solid line: criteria of absolute instability for free shear layer [30].

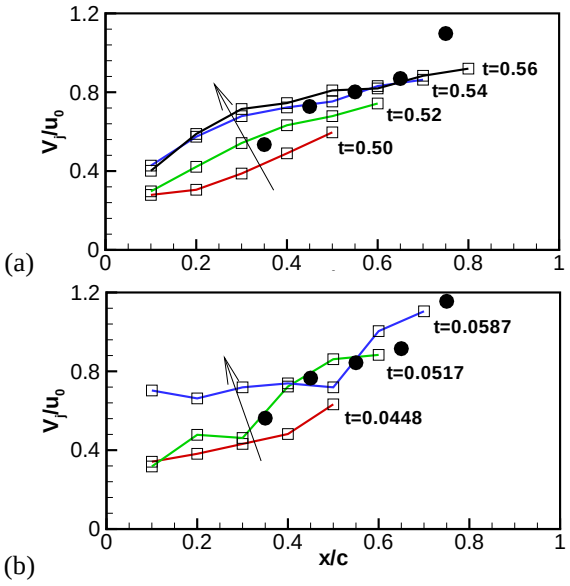

Figure 16. Instantaneous re-entrant jet velocity magnitude as a function of distance from the leading edge with time increment; (a) dynamics 1 (AOA=6 deg. σ=1.05). (b) dynamics 2 (AOA=8deg. σ=1.27). Filled symbols are time-averaged measurments of Pham et al. for different hydorfoil [2].

of Coutier-Delgosha et al., present computations well reproduced steady/unsteady partial cavitating flows observed in experiments of Leroux et al. The present numerical simulations well captured the unsteady mode of unstable partial sheet cavity and subsequent cloud cavitation not only qualitatively but also quantitatively. The high & low frequency modes of cloud cavitation observed in the experiments for two different angle of attack are also found in the present computations. Thus, the present numerical model predicts many observed macro-scale features of the unsteady cavitating flow on a hydrofoil section, though it depends on empirical models. With the aid of high-order numerical methods, pressure waves generated by cloud cavitation are resolved and presented. Some features on the measured pressure signal are qualitatively explained with the resolved pressure wave phenomena. The re-entrant jet flow which is responsible for the destabilization of partial sheet cavity is also closely investigated. Although the present computation is performed with a RANS type turbulence model, the instability on the shear layer formed by strong re-entrant jet flow is clearly observed. Finally, the mechanism which is responsible for two different unsteady modes of cloud cavitation is studied, and the different strength of pressure wave generated by cloud collapse and a flow-blockage effect caused by the large vortical structure of cloud are identified. The results of present numerical simulation conducted with the simplification of 2D assumption and RANS modeling are validated by the comparison with the experiments, and give

some insight of detailed flow features and wave phenomena. A 3D computation with turbulent eddy resolution (LES/DNS) can allow the investigation of detailed flow features and understanding of related physics involving the coupling between turbulence and cavitation phenomena possible.

ACKNOWLEDGMENT

The authors wish to express gratitude to Prof. J.-A. Astolfi at Institut de Recherche de l'Ecole Navale, France for kindly providing the experimental data. This work is supported by the Korea Research Foundation Grant funded by Korea Government (MOEHRD) : KRF-2007-357-D00036. Partial support from DOE SciDAC-II (S. K. Lele, PI) is also gratefully acknowledged. This support allowed the work reported here to be completed.

REFERENCES

[1] Kawanami, Y., Kato, H., Yamaguchi, H., Tagaya, Y., and Tanimura, M., 1997 "Mechanism and Control of Cloud Cavitation," *J. Fluids Eng.* 119, 788.

[2] Pham, T. M., Larrarte, F., and Fruman, D. H., 1999 "Investigation of Unsteady Sheet Cavitation and Cloud Cavitation Mechanisms," *J. Fluids Eng.* 121, 289.

[3] Arndt, R. E. A., Song, C. C. S., Kjeldsen, M., He, J., and Keller, A., 2000 "Instability of Partial Cavitation: a Numerical/Experimental Approach," *Proc. of 23rd Symposium on Naval Hydrodynamics, ONR, Val de Reuil, France,* 599-615, pp. 599-615.

[4] Reisman, G. E., Wang, Y.-C., and Brennen, C. E., 1998 "Observation of Shock Wave in Cloud Cavitation," *J. Fluid Mech.*355.

[5] Leroux, J-B., Astolfi, J-A., and Billard, Y., 2004 "An Experimental Study of Unsteady Partial Cavitation," *J. Fluid Eng.* 126, 94.

[6] Leroux, J-B., Coutier-Delgosha, O., and Astolfi, J-A., 2005 "A Joint Experimental and Numerical Study of Mechanism associated to Instability of Partial Cavitation on Two-dimensional Hydrofoil," *Phys. Fluids* 17

[7] Leroux, J-B., 2003 "Etude Experimentale En Tunnel Hydrodynamique Des Instabilites De La Cavitation Par Poche Sur Hydrofoil Par La Mesure Spatio Temporelle Du Champ De Pression Parietal," *Doctoral Thesis, L'Ecole Centrale de Nantes et l'Universite de Nantes*

[8] Shin, B. R., Iwata, Y., and Ikohagi, T., 2003 "Numerical Simulation of Unsteady Cavitating Flows using a Homogeneous Equilibrium Model,"

[9] Lele, S. K., 1992 "Compact Finite Difference Scheme with Spectral-like Resolution," *J. Compt. Phys.* 103,1, pp. 16-42.

[10] Cook, A. W. and Cabot, W. H., 2005 "Hyper Viscosity for Shock-turbulence Interactions," *J. Compt. Phys.* 203,2, pp. 379-385.

[11] Fiorina, B. and Lele, S. K., 2007 "An Artificial Nonlinear Diffusivity Method for Supersonic Reacting Flows with Shocks," *J. Compt. Phys.* 222, pp. 246-264.

[12] Kawai, S. and Lele, S. K., 2008 "Localized Artificial Diffusivity Scheme for Discontinuity Capturing on Curvilinear meshes," *J. Compt. Phys.* 227, 22.

[13] Spalart, P. R. and Allmaras, S. R., 1992 "A One-Equation Turbulence Model for Aerodynamics Flows," *AIAA-Paper* 92-0439.

[14] Coutier-Delgosha,O., Reboud, J. L., and Delannoy, Y., 2003 "Numerical Simulation of the Unsteady Behavior of Cavitating Flows," *Int. J. Numer. Meth. Fluids* 42, pp. 527-548.

[15] Coutier-Delgosha, O., Fortes-Patella, R., and Reboud, J. L., 2003 "Evaluation of Turbulence Model Influence on the Numerical Simulation of Unsteady Cavitation," *J. Fluid Eng.* 125, pp. 38-45.

[16] Zhou, L. and Wang, Z., 2008 "Numerical Simulation of Cavitation around a Hydrofoil and Evaluation of a RNG k-ε Model," *J. Fluid Eng.* 130.

[17] Seo, J. H., Moon, Y. J., and Shin, B. R., 2008 "Prediction of Cavitating Flow Noise by Direct Numerical Simulation," *J. Compt. Phys.* 227, pp. 6511-6531.

[18] Saito, Y., Takami, R., Nakamori, I., and Ikohagi, T., 2007 "Numerical Analysis of Unsteady Behavior of Cloud Cavitation around a NACA0015 Foil," *Compt. Mech.* 40, pp. 85-96.

[19] Iga, Y., Nomi, M., Goto, A., and Ikohagi, T., 2004 "Numerical Analysis of Cavitation Instabilities arising in the Three-Blade Cascade," *J. Fluid Eng.* 126, pp. 419-429. *Compt. Mech.* 30, pp. 388-395.

[20] Chen, H. T. and Collins, R.,1971 "Shock Wave Propagation Past an Ocean Surface," *J. Compt. Phys.* 7, pp. 89-101.

[21] Akagawa, K., 1974 "Gas-liquid Two-Phase Flow," *Tokyo: Corona Pub.*

[22] Sone, Y., and Sugimoto, H., 1990 "Adiabatic Waves in Liquid-Vapor Systems," *Springer, Berlin Heidelberg NewYork* pp. 293-304.

[23] Beattie, D. R. H. and Whalley, P. B., 1982 "A Simple Two-phase Fractional Pressure Drop Calculation Method," *Int. J. Multiphase Flow* 8, pp. 83-87.

[24] Gaitonde, D., Shang, J. S., and Young, J. L., 1999 "Practical Aspects of Higher-order Accurate Finite Volume Schemes for Wave Propagation Phenomena," *Int. J. Numer. Meth. Eng.* 45, pp. 1849-1869.

[25] Freund, J. B., 1997 "Proposed Inflow/Outflow Boundary Condition for Direct Computation of Aerodynamic Sound," *AIAA Journal* 35,4, pp. 740-742.

[26] Song, C. C. S., and Qin, Q., 2001 "Numerical Simulation of Unsteady Cavitating Flows," *CAV 2001, Fourth Int. Symp.*

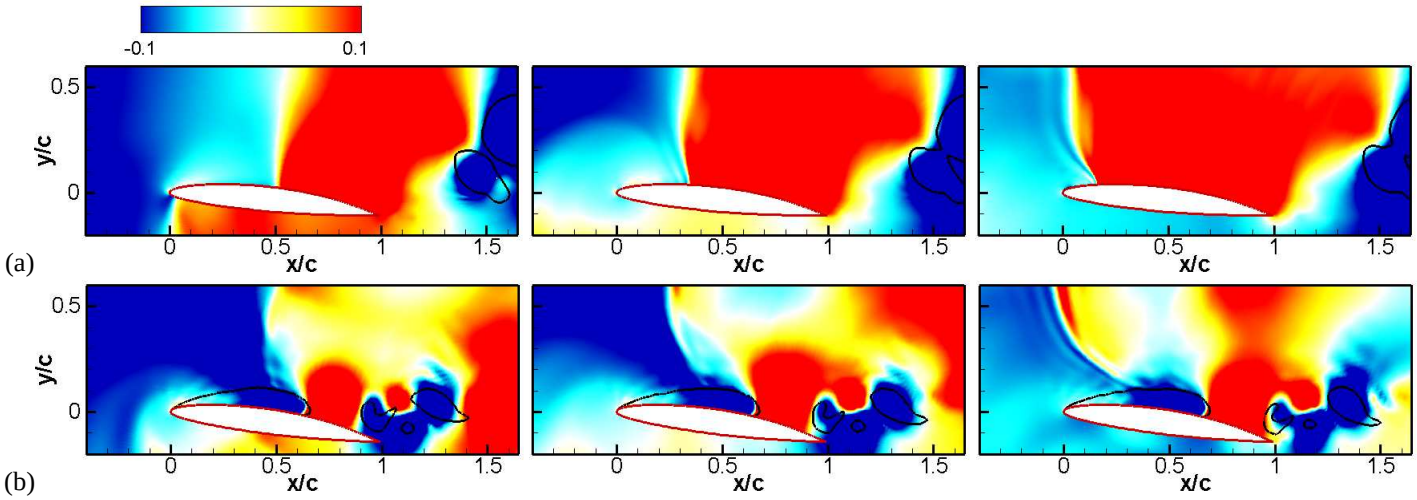

Figure 17. Pressure wave propagating to upstream. Non-dimensionalized pressure fluctuation, $(p-\bar{p})/\rho_0 u_0^2$ contours. Black line represents cavity shape; (a) Dynamics 1, AOA=6 deg. σ=1.05, During frame (j)-(k) of Fig.10. (b) Dynamics 2, AOA=8 deg. σ=1.27, During frame (h)-(a) of Fig.12.

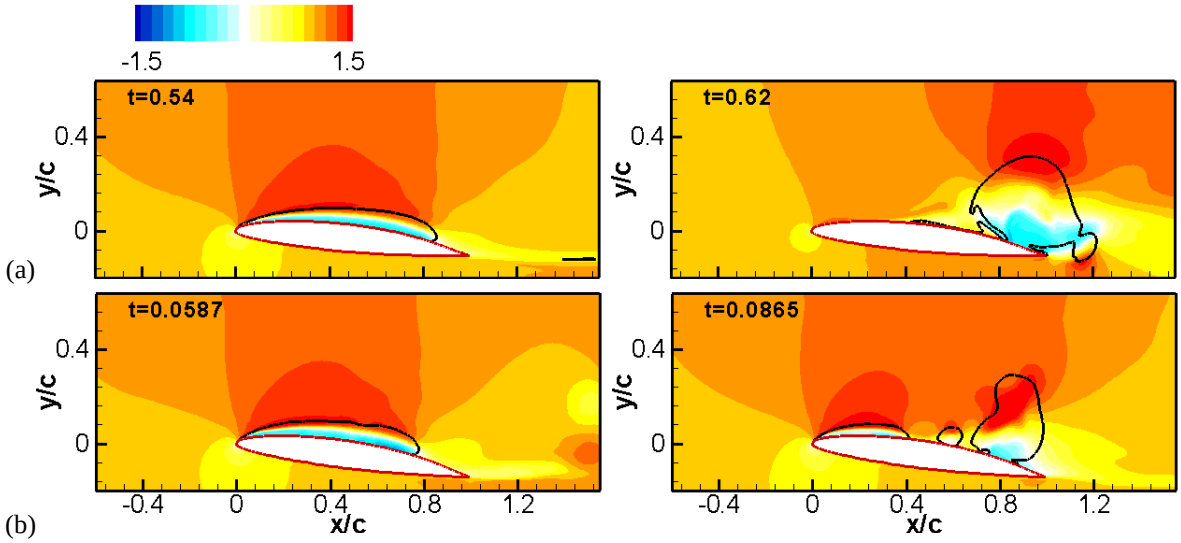

Figure 18. Streamwise velocity u/u_0 contours. Black line represnets cavity shape, (a) Dynamics 1, AOA=6 deg. σ=1.05, (b) Dynamics 2, AOA=8 deg. σ=1.27, Left: When sheet cavity is developing, Right: When it rolled-up into cloud.

on Cavitation, June 20-23, Pasadena, CA.

[27] Avellan, F., Dupont, P., and Ryhming, I., 1988 "Generation Mechanism and Dynamics of Cavitation Vortices Downstream a Fixed Leading Edge Cavity," *Proc. of the 17th Symp. on Naval Hydrodynamics*, pp. 317-329.

[28] Kjeldsen, M., 1997 "Theoretical and Experimental Investigations of the Instabilities of an Attached Cavity," *Proc. of the ASME Fluids Engineering Division Summer Meeting*.

[29] Huerre, P. and Monkewitz, P. A., 1985 "Absolute and Convective Instabilities in Free Shear Layers," *J. Fluid Mech.*, 159, 151-168.

[30] Jendoubi, S. and Strykowski, P. J., 1994 "Absolute and Convective Instability of Axisymmetric Jets with External Flow," *Phys. Fluids*, 6, 9.